



Characterization and optical properties of reduced graphene oxide doped nano-crystalline vanadium pentoxide

M. M. El-Desoky¹ · M. M. Abdulrazek¹ · Y. A. Sharaby¹

Received: 18 January 2020 / Accepted: 28 May 2020 / Published online: 6 June 2020
© Springer Science+Business Media, LLC, part of Springer Nature 2020

Abstract

In this paper, the structural and optical properties of reduced graphene oxide (rGO) doped vanadium pentoxide nanocrystalline films were studied. rGO was synthesized using modified Hummer method and confirmed by EDX, XRD and HRTEM. XRD measurements showed good fit with known card JCPDS 40-1296 of vanadium pentoxide with nanocrystals structure oriented toward the *c*-axis. The line of (002) in XRD graphs is getting weaker by the addition of rGO till nearly missing at the higher concentrations indicating intercalation of rGO within the vanadium layers. The average particle size measured decreased with increasing rGO content from 4.86 to 3.17 nm. Optical properties were studied by measuring the absorption, reflectance and transmittance of the prepared samples using double-beam UV–Vis spectrophotometers. The optical constants like refractive index *n*, extinction coefficient *k*, real and imaginary dielectric constants, absorption coefficient α , and optical band gap E_{op} of the nanocrystalline films have been evaluated. The absorption coefficient decreases with increasing rGO content, which may be attributed to decrease in lattice distortion owing to rGO content due to the decrease of particle size as indicated in the XRD and HRTEM. Optical measurements revealed that there are two different optical gaps present. The optical gap E_{op1} was found to decrease with increase in rGO content, while the optical gap E_{op2} was found to increase with increase in rGO content. The carrier's concentrations as well as the effective mass were calculated assuming hydrogen-like model. The good absorption in the UV region of $rGO_xV_2O_5 \cdot nH_2O$ films are promising candidate for solar cell photostabilizer applications.

Keywords Vanadium pentoxide · Reduced graphene oxide · Sol–gel thin nanocrystalline films

This article is part of the Topical Collection on Advanced Photonics Meets Machine Learning.
Guest edited by Goran Gligoric, Jelena Radovanovic and Aleksandra Maluckov.

✉ M. M. El-Desoky
mmdesoky@gmail.com; mmdesoky@suezuniv.edu.eg

¹ Physics Department, Faculty of Science, Suez University, Suez 43518, Egypt

1 Introduction

Nowadays, transparent electronics devices are the center of interest in many applications. Many materials are a good candidate and one of them is oxides based on vanadium as it is a promising transparent oxide semiconductors (TOS) (Prociow et al. 2011). Vanadium oxides are one of the best candidates due to the layered structures, which are well known to intercalate water molecules between the layers (McNulty et al. 2019). The structural model for the V_2O_5 xerogel, proposed by Legendre et al. (1983) and Yao and Oka (1997) has a lamellar structure, as shown in Figs. 1 and 2, respectively which is a distorted orthorhombic structure. This distortion is the main producer of sheet like shapes.

Sol–gel methods is a preferred synthetic process as it offers creating an optical material with much different properties compared to other traditional chemical solid-state methods (Klein 2013; Al-Assiri et al. 2010). This is because solid-gel synthesis is distinguished by lower synthesis temperature, homogeneous mixing at the atomic level, better crystallinity and uniform particle size at the nanometer level.

Making thin films of nanocrystalline material can be easily achieved using the sol–gel technique. And vanadium pentoxide gels are a good candidate for optical and electronic devices (Ramana et al. 1997; Bahgat et al. 2011; Mady et al. 2012) as it exhibits its semiconducting properties from electron transfer between V^{4+} and V^{5+} ions (Wright 1984; Takeda et al. 1996).

Fig. 1 Structural model for the V_2O_5 xerogel, proposed by Aldebertetal

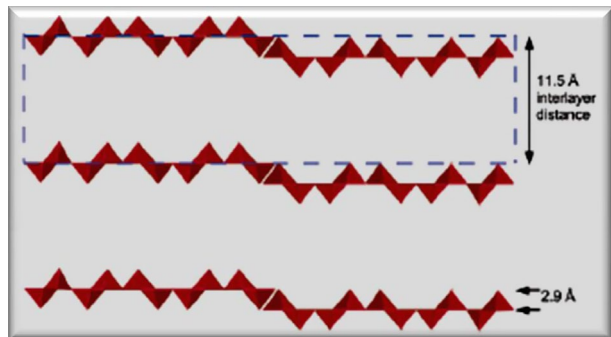
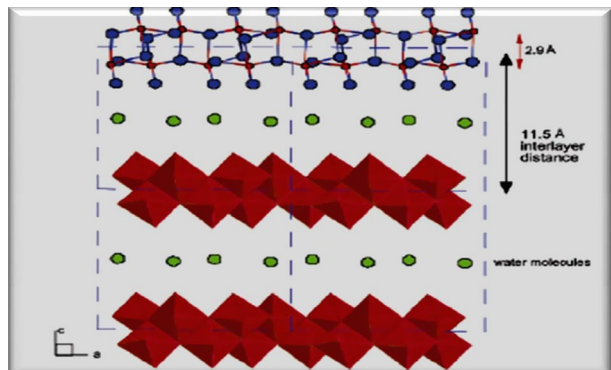


Fig. 2 Structural model for the V_2O_5 xerogel, proposed by Yao et al.



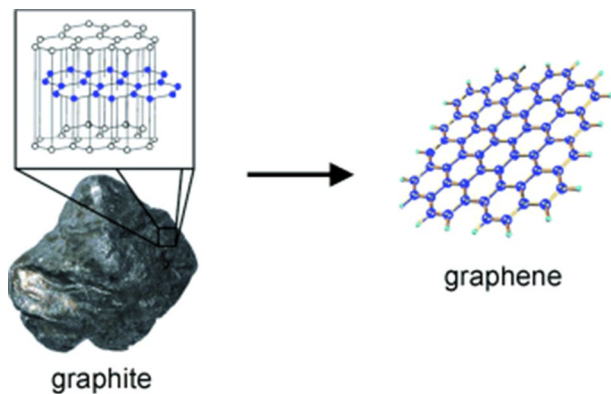
The optical transmittance spectrum of V_2O_5 sol–gel exhibit a characteristic absorption band at a wavelength of about 500 nm and it has a steady transmittance of 75% in the visible region. The absorption edge at 2.3–2.5 eV in vanadium–oxygen compounds is ascribed to $O2p \rightarrow V3d$ electron transitions and it is consistent with the energy gap of V_2O_5 , $E_{op} = 2.35$ eV, and $V_2O_5 \times nH_2O$, $E_{op} = 2.49$ eV (Ganeshan et al. 2016; Kazakova et al. 2014; Pergament et al. 2002).

Graphene is a 2D material with one atom thick carbon sheet. The atoms are arranged in a honeycomb-shaped structure made of hexagons. They can be imagined as a composed of benzene rings after being stripped out from their hydrogens (see Fig. 3) (Randviir et al. 2014). Graphene has many unique properties such as zero band gap with extremely high intrinsic carrier mobility ($20,000 \text{ cm}^2/\text{V s}$), high chemical stability and superior optical and thermal properties (Wang et al. 2018). Graphene also has a tremendously high optical transparency that can reach up to 97.7% for monolayer (or low optical absorptivity for a monolayer as low as 2.3%) (Randviir et al. 2014). The origin of the unique optical properties can be defined by the fundamental constants lies in the two-dimensional nature of this material combined with the gapless electronic spectrum of graphene and does not directly involve the chirality of its charge carriers (Wang et al. 2018).

Nowadays, graphene is considered a promising material for many application fields including optics. For example, Li et al. have synthesized NiS_2 /reduced graphene oxide (rGO) nanocomposite for an efficient dye-sensitized solar cells (DSSCs) (Li et al. 2013). The composite material showed higher performance than individual components due to the synergetic effect between metal compounds and graphene sheets. Also, M. Lee and S. K. Balasingam, used graphene modified vanadium pentoxide nanobelts as an efficient counter electrode for dye-sensitized solar cells (DSSCs) (Lee et al. 2016a).

In this work, our aim is to study the change in the nano-structural and optical properties in the visible and near infrared regions of vanadium pentoxide films after being doped with reduced graphene oxide (rGO) in the form of $xrGO (x - 1)nH_2OV_2O_5$ where $x = 0, 0.05, 0.10, 0.20, 0.25$ and 0.35 mol%. The films were formed on glass substrate by sol–gel method.

Fig. 3 Graphite and graphene



2 Experimental

The modified Hummer method was used to synthesize the rGO. Started by preparing an ice dipped container then adding 5 g of extra pure graphite to 2.5 g sodium nitrate (NaNO_3) in 110 ml H_2SO_4 and cooling to 0° using the ice. Then stirring and slowly adding 15 g of potassium permanganate (KMnO_4) while controlling the heat not exceeding 20°C by controlling the adding rate. Then adding 1.5 L of H_2O slowly and watch the temperature rises up to 98°C . Start treating by adding 200 ml of 30 mol% hydrogen peroxide (H_2O_2) to reduce the residual of KMnO_4 then washing and drying to get Graphene oxide powder (GO). Sonicating in 20 ml H_2O until yellow dispersion is obtained then adding 40 ml of hydrazine hydrate (HH) as a reducing agent. After that, the solution was microwaved for 60 s till the yellow dispersion turns to black indicating the reduction to reduced graphene oxide (rGO).

Five different samples, of $x\text{rGO}-(1-x)\text{V}_2\text{O}_5\cdot n\text{H}_2\text{O}$ ($x=0.05, 0.10, 0.20, 0.25$ and 0.35 mol%) were proposed for the present investigation. Then for each sample, added the doping weight of rGO to 5 ml of H_2O and sonicated for 1 h. Then for each sample, adding 1 g of pure V_2O_5 to 30 ml of 5% H_2O_2 while stirring and keeping the mixture at $55\text{--}60^\circ\text{C}$. Just before gelation starts, we slowly add the sonicated rGO. Nanocrystalline films made by dipping technique were obtained for each concentration (see Fig. 4).

For XRD analysis, we used SIEMENS D5000 X-ray Diffractometer (with Cu-K α radiation and $\lambda=1.5406$). The diffraction data were recorded for 2θ between 5° and 60° with a resolution of 0.05. The resulted graphs were processed and compared with international database by pattern recognition software "X'Pert HighScore[®]" which identifies the existing planes, crystal structure and the interplanar spacing. Furthermore, graph analysis software, Origen[®], was used to analyze the peaks and their full width half maximum (FWHM) to calculate the average particle size using Scherrer method for each rGO concentration.

TEM for present samples were analyzed by JEOL JEM-2100 TEM. For each sample, the general structure, particle size and EDX was analyzed.

For the optical properties we used SHIMADZU UV-2600 spectrophotometer operating from UV region ($\lambda=200$ nm) to IR region ($\lambda=1200$ nm). The prepared samples were tested for optical transmittance (T), absorption (A) and reflectance (R) at room temperature. Slit width or signal amplification gain is controlled automatically to adjust the base line before any series of measurements. Then, film thickness (t), was obtained using SWANEPOEL method (Sánchez-González et al. 2006; Li et al. 2009; Caglar et al. 2006). Other optical parameters for different doping concentrations were investigated

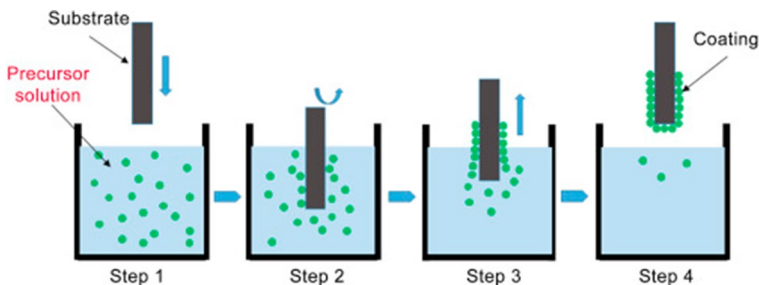


Fig. 4 Dip coating illustration

including optical direct and indirect band gap, Urbach activation energy, the dissipation factor ($\tan \delta$), surface energy loss, volume energy loss, dispersion energy parameters and real ϵ' and imaginary ϵ'' parts of the dielectric constant.

3 Results and discussion

3.1 XRD analysis

The resulted x-ray diffraction for the prepared samples are illustrated in in Fig. 5 were the highest intensity peak is related to (001) plane appearing at 2θ of 6.8–7.2. Other peaks related to (002), (003), (004) and (005) are appearing with good fit with vanadium pentoxide xerogel card number 00-040-1296 or/(JCPDS 40-1296) with Orthorhombic crystal system (Al-Assiri et al. 2010; Li et al. 2014). However, peak (002) is weak or missing in higher rGO concentrations.

From XRD analysis, the obtained nanocrystalline films were found to be highly orientated nanocrystals with their c-axis normal to the substrate surface (Bahgat et al. 2005). The (0 0 2) line is weak in the pure V_2O_5 sample as a result of the layer structure of the nanocrystalline films and gets from weaker to missing as the rGO increases, which facilitates a layer of intercalation.

The average particle size (D) of nanocrystalline films was calculated by Scherrer equation, Eq. (1)

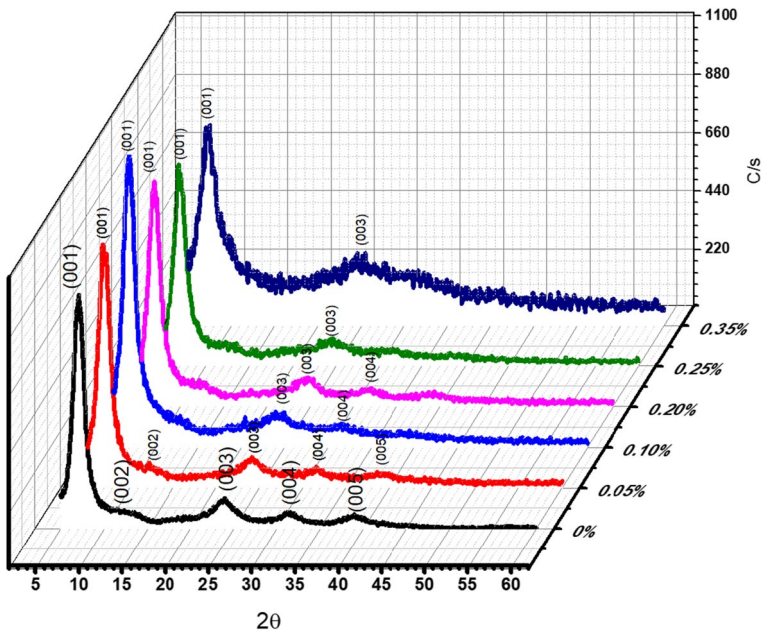
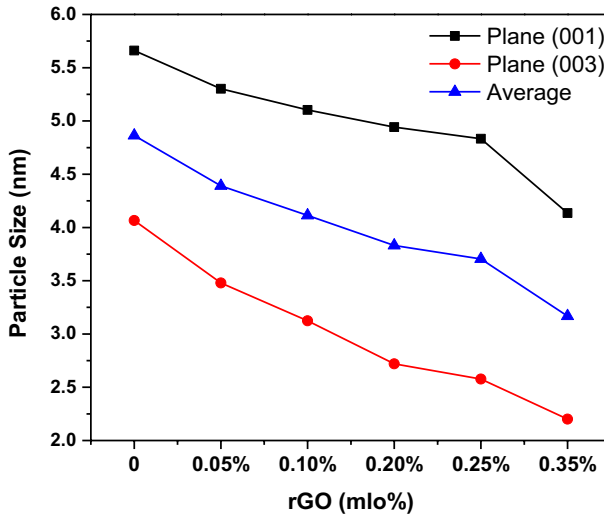


Fig. 5 Room-temperature XRD for different rGO content in the relevant angles (2θ)

Table 1 Particle size in (nm) calculated for different rGO content

Sample	Pure	0.05 mol%	0.10 mol%	0.20 mol%	0.25 mol%	0.35 mol%
[r-GO/V ₂ O ₅] mol ratio	0	0.0005	0.0010	0.0020	0.0025	0.0035
Peak [001]	5.66	5.30	5.10	4.94	4.83	4.14
Peak [003]	4.07	3.48	3.12	2.72	2.58	2.20
Average D (nm)	4.86	4.39	4.11	3.83	3.70	3.17

**Fig. 6** Particle size for different rGO content

$$D = \frac{k\lambda}{\beta \cos\theta} \quad (1)$$

where $k \sim 1$, $\lambda = 1.5406 \text{ \AA}$ for Cu ($K\alpha$), β is the full width at half maximum (FWHM) in radians and θ is Bragg angle (Bartram and Kaelble 1967). We used the Gauss fitting method from Origin[®] software for the main peaks (001) and (003) to calculate the particle size. Table 1 contains the calculated particle size from both planes (001) and (003). The average particle size decreased with increasing the amount of rGO from 4.86 to 3.17 nm as indicated in Fig. 6.

3.2 HRTEM

The structural information of the prepared samples with rGO of 0.10 mol%, 0.20 mol% and 0.35 mol% are obtained from high resolution transmission electron microscope (HRTEM) observation. Figures 7 and 8 show HRTEM images for representative samples 0.10 mol%, 0.20 mol% and 0.35 mol%.

Figure 7a–f taken at 100 nm and 200 nm scale shows vanadium layers penetrated by rGO. And in Figs. 7b and 6d at a scale of 200 nm, showing large sheet of graphene

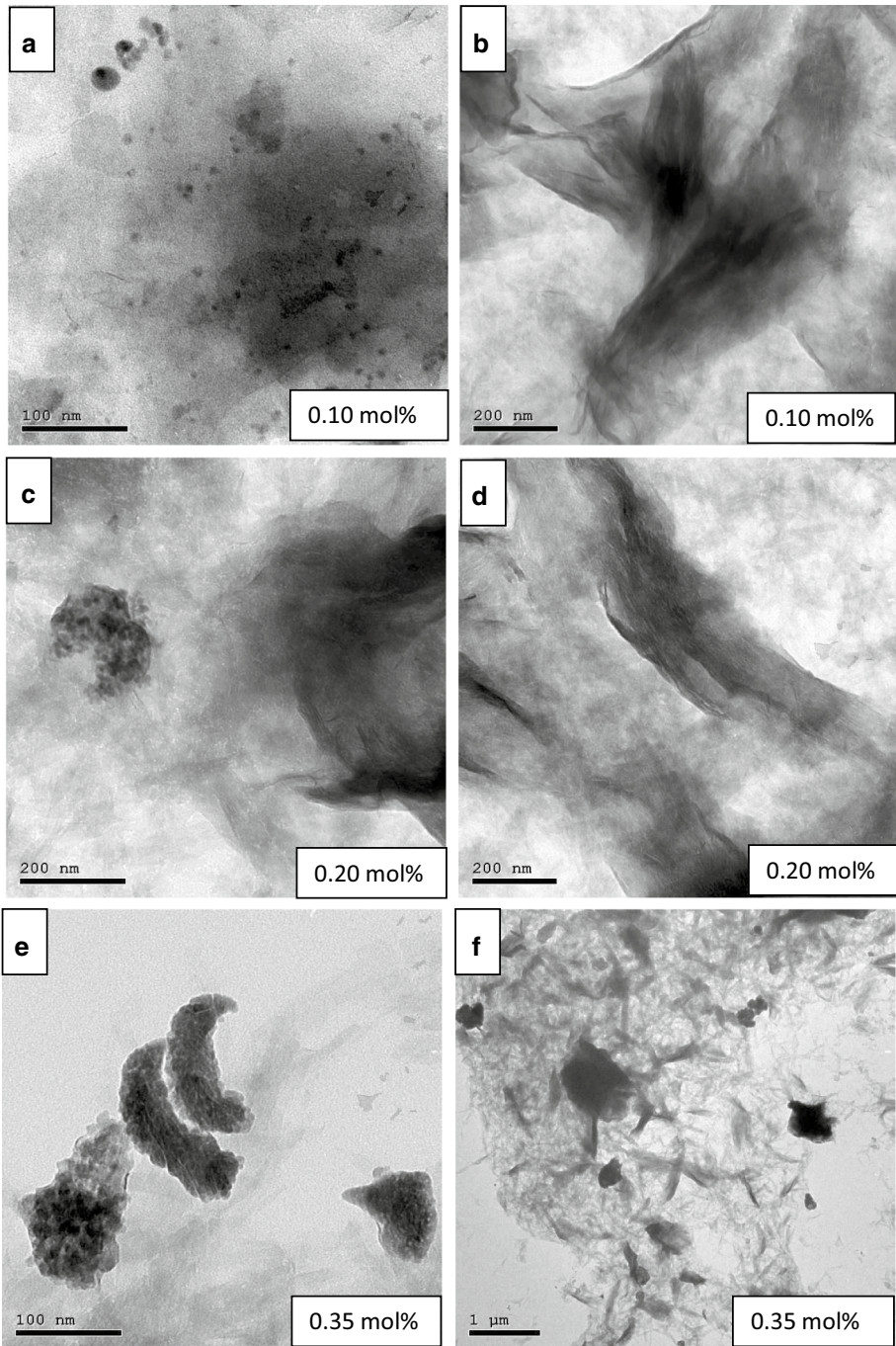


Fig. 7 a–f HRTEM at 100 nm and 200 nm scale

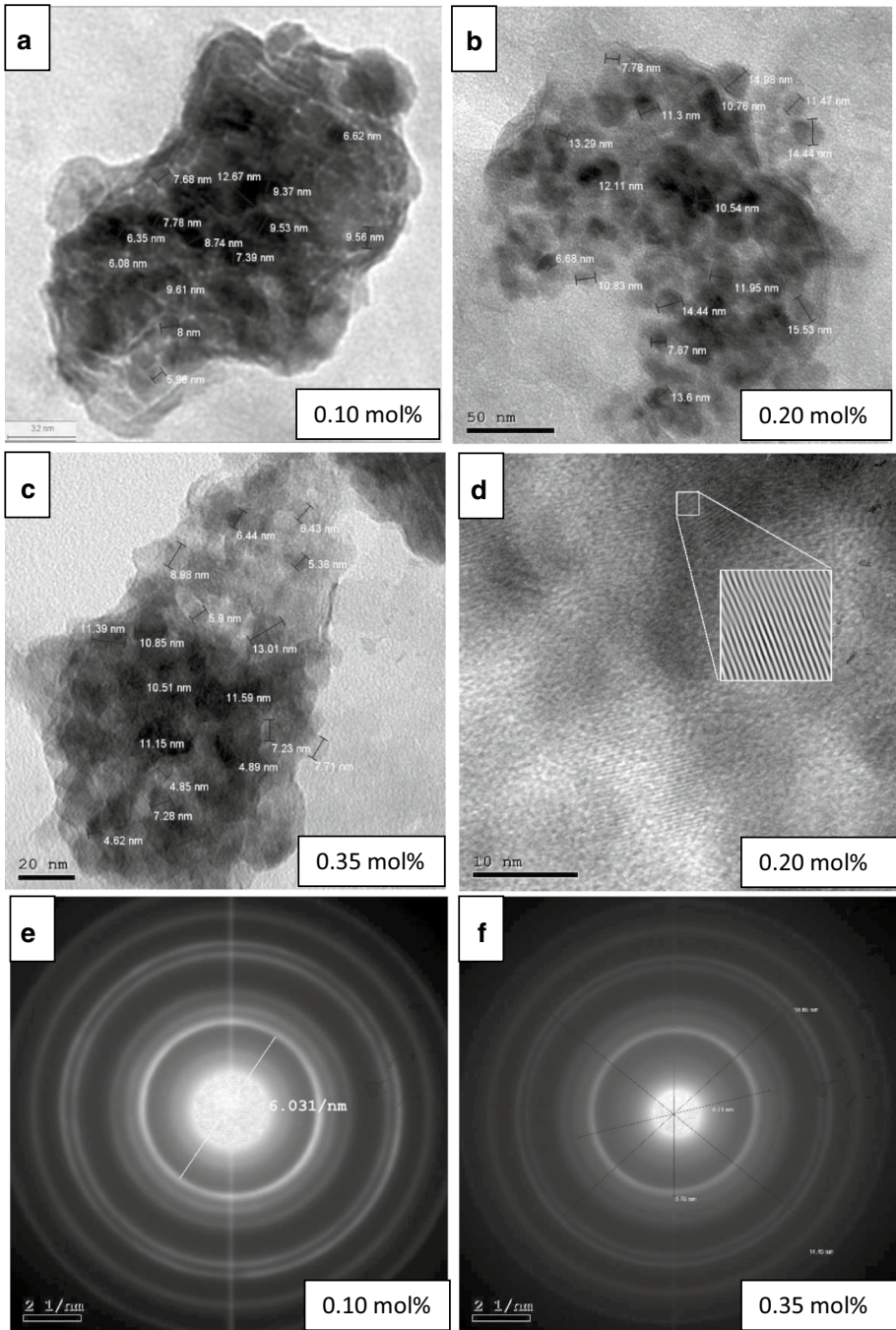


Fig. 8 a–c HRTEM of measured particle size, **d** interplanar spacing (d-spacing) for 0.20 mol% and **e, f** SAED for 0.10 mol% and 0.35 mol%

almost 1000 nm wide. In Fig. 7f, a large rGO sheet at the scale of micrometer appears penetrating the vanadium layers. This indicated the successful of preparation of rGO sheets inset vanadium layers.

The particle size was measured as indicated in Fig. 8a–c showing particle size measured from 4.62 to 5.96 nm which agrees with calculated particle size from XRD analysis.

Figure 8d shows clear lattice fringes of 0.20 mol% sample implying high nanosheet crystallinity. It brings out a lattice spacing of ~0.422 nm which is related to (003) plane which correspond to c-axis and which is higher than that calculated from X-ray diffraction of (003) plane (0.361 nm). This can be explained by the effect of structured water due to the sample preparation of HRTEM which involves dissolving in water (Zheng et al. 2017).

The inset of Fig. 8e, f shows the corresponding selected area electron diffraction (SAED) pattern of 0.10 mol% and 0.35 mol% samples. The diffraction spots match in good agreement with the JCPDS file (40-1296) (Nagaraju et al. 2014).

3.3 Film thickness

The film thickness (t) was calculated using SWANEPOEL method (Sánchez-González et al. 2006; Li et al. 2009; Caglar et al. 2006). This method calculates the thickness by analysing the envelop of the transmittance spectrum and perform theoretical calculations which takes into account the interference effects. Where (t) is film thickness, (n) is a complex refractive index and (k) is extinction coefficient that is expressed in the terms of the absorption coefficient (α). The substrate has a thickness of several orders of magnitude larger than that of the film and a refractive index (s). As the interference phenomena between the wave fronts generated at the two interfaces (air and substrate), defines the sinusoidal behavior of the curves' transmittance versus wavelength of light (Aristizábal and Mikán 2016). Using Origin[®] signal processing tools to draw curve envelop T_{\max} and T_{\min} are the transmissivity envelope curve maximum and the minimum of the normal incidence transmitted spectrum where N is defined according to Eq. (2) to be:

$$N = \frac{1}{2}(1 + S^2) + 2S(T_{\max} - T_{\min}) / (T_{\max} * T_{\min}) \quad (2)$$

and s is the refractive index of glass substrate (1.52). The thickness of the nanocrystalline films was calculated using Eq. (3) as following:

$$t = \frac{\lambda_1 \lambda_2}{2(\lambda_1 n_2 - \lambda_2 n_1)} \quad (3)$$

Applying the above given method nanocrystalline films thicknesses are evaluated accordingly and given in Table 2.

Table 2 Film thickness for different rGO content

Sample	0 mol%	0.05 mol%	0.10 mol%	0.20 mol%	0.25 mol%	0.35 mol%
t (μm)	1.391	1.649	1.877	1.679	2.304	2.165

3.4 Spectral distribution and the absorption coefficient α

In the present work, absorption, A , transmittance, T and reflectance, R , spectra were measured at room temperature as a function of wavelength in the range from 200 to 1200 nm as indicated in Fig. 9a–c, respectively.

In Fig. 9a, from 200 to 500 nm, the absorptivity decreases with the increase of the rGO but without any shift in wave lengths lower than 500 nm. This indicates good absorption in the UV region which can rather be used as good candidate for solar cell photostabilizer applications (Lee et al. 2016b; Roose et al. 2016, 2018). The decrease in absorption after adding rGO is attributed as multi-layered graphene has lower absorption intensity compared to single and double layers (Zhao et al. 2012). On the other hand, the addition of low absorption rGO and high-transparent ~97.7% replacing of high-absorbing V_2O_5 reduces absorption with increased rGO (Brownson et al. 2012). In Fig. 9b, the transmittance can also be divided into two regions, from 200 to 500 nm, the transmittance increases with the increase of rGO, while from 500 to 1200 nm, the transmittance decreases with the increase of rGO. Also, the transmittance is generally higher in the region from 500 to 1200 nm than from 200 to 500 nm. This property shows that transmittance for certain wavelengths can be controlled by the addition of rGO.

Figure 9c, shows that the reflectance generally decreases by the increase of rGO content specially in the lower wavelength region up to 500 nm. This overlapping behavior is typical for vanadium pentoxide nanocrystalline films as noticed in other papers (Dultsev et al. 2006; Abyazisani et al. 2015; Tashtoush and Kasasbeh 2013). The tendency of reflectance to decrease with replacing of high-reflectance V_2O_5 by low reflectance rGO reduces reflectance with rGO content. On the other hand, the tendency of the reflectance to decrease with the addition of rGO is related to the increase of number of layers of rGO (Ghamsari et al. 2016).

The absorption coefficient (α) for the prepared nanocrystalline films was calculated using Eq. (4)

$$\alpha = \frac{2.303 * A\%}{\text{Thickness (t)}} \quad (4)$$

The result of (α) as a function of E (eV) for the present samples are illustrated in Fig. 10.

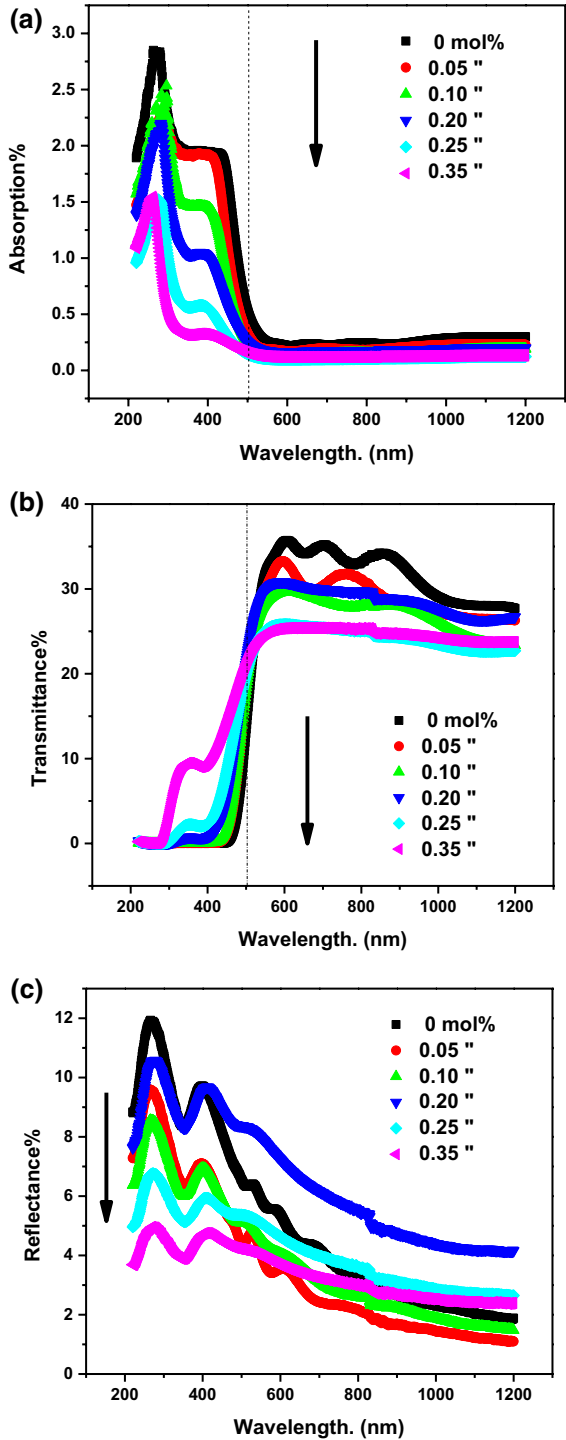
The absorption coefficient decreases with increasing rGO content, which may be attributed to decrease in lattice distortion owing to rGO content due to the decrease of particle size as indicated in the XRD and HRTEM (Gupta and Ramrakhiani 2009).

3.5 Studying extinction coefficient k and refractive index n

The obtained curves of T and R for prepared nanocrystalline films were used to compute n and k . The extinction coefficient k , represents the light fraction which lost due to scattering and absorption per unit distance of the penetrated medium. Where α and k are related by Eq. (5) (Al-Assiri et al. 2010; Tashtoush and Kasasbeh 2013; El-Desoky et al. 2018) and k is illustrated in Fig. 11a.

$$k = \frac{\alpha \lambda}{4\pi} \quad (5)$$

Fig. 9 **a** Absorption, **A**, **b** transmittance, **T** and **c** reflectance, **R**, spectra for different rGO content



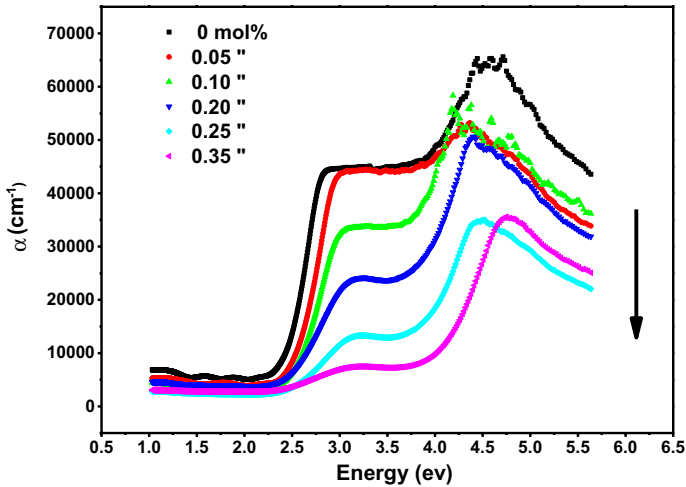


Fig. 10 Absorption coefficient (α) as a function of photon energy

While the refractive index n can be calculated according to the following, assuming normal incidence, the reflection coefficient affecting the intensity of the radiation is given by Eq. (6) and illustrated in Fig. 11b.

$$n = \frac{(1 + \sqrt{R})}{(1 - \sqrt{R})} \quad (6)$$

It is clearly showing from the curves that k decreases with the increasing of rGO. This is a predicted behavior as k is directly proportional to the A which also decreases with increasing the rGO content. The refractive index of samples exhibit slightly variation with rGO content which can be attributed to the increase of rGO layers intercalated between V_2O_5 layers which as similar behavior for refractive index of graphene and reduced graphene oxide was found in other researches (Arefinia et al. 2013; Schmie-dova et al. 2017; Matkovic and Gajic 2013). In general, the refractive index behavior is derived by the reflectance as indicated by Eq. (6).

3.6 Determining the optical band gap (E_{op})

The optical band gap E_{op} is the gap corresponds to the minimum energy difference between the bottom of the conduction band and the top of the valance band take place. This gap also depends on the transitions between extended states in both valence and conduction bands. For a semiconductor to become nanocrystalline, the absorption edge may get shifted toward either lower or higher energies. Also, in some cases, extended new edges are formed and observed.

The absorption spectrum can be divided into three regions according to the magnitude of the measured absorption coefficient α .

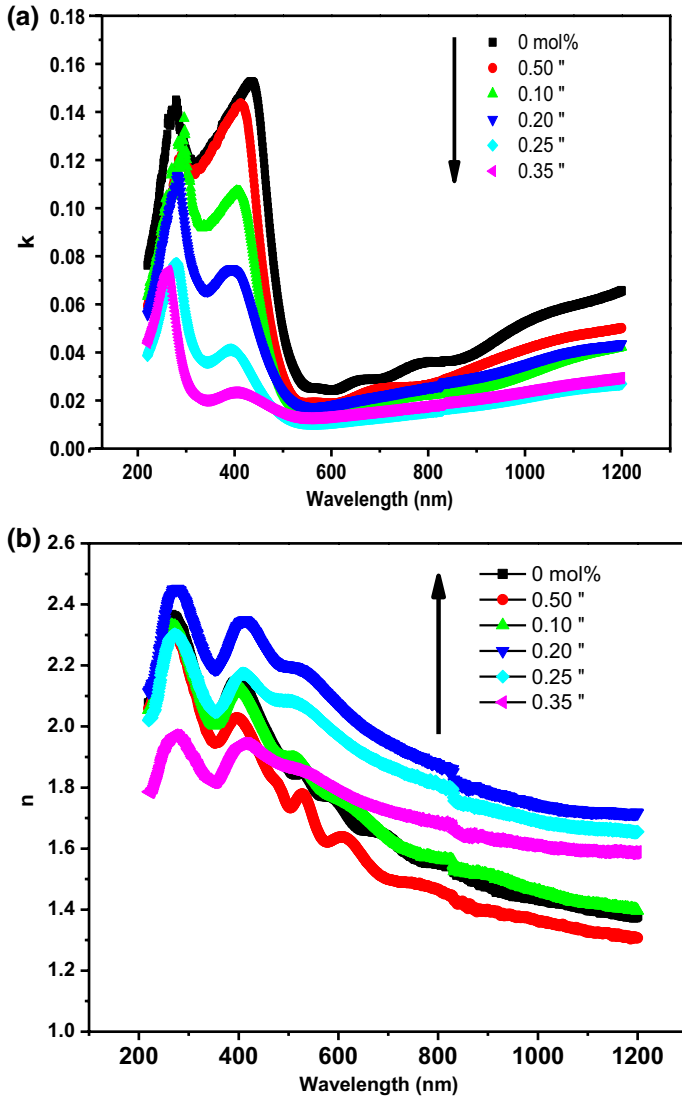


Fig. 11 a Extinction coefficient (k), b refractive index (n) as a function of wavelength λ

- 1 A high absorption region ($\alpha > 10^4 \text{ cm}^{-1}$) where band gap is related to the absorption coefficient α using Tauc's equation (Tashtoush and Kasasbeh 2013; Ghobadi 2013):

$$\alpha h\nu = \beta(h\nu - E_{op})^m \tag{7}$$

Where β is the band edge width parameter related to the quality of the film and m is a parameter representing the type of the optical transition as following:

$m = 1/2$ for direct allowed transition, $m = 3/2$ for direct forbidden transition
 $m = 2$ for indirect allowed transition, $m = 3$ for indirect forbidden transition

- 2 An intermediate absorption region (where $1 \text{ cm}^{-1} < \alpha < 10^4 \text{ cm}^{-1}$), or ($50 < \alpha < 5 \times 10^3$). Where the absorption is directly depending on the photon energy and obeys Urbach's empirical equation (Studeniyak et al. 2014):

$$\alpha = \alpha_o \exp \frac{h\nu}{E_e} \tag{8}$$

where E_e is Urbach energy representing the width of the band tail which is formed due to localized states at the band tail which represents the degree of disorder in an amorphous semiconductor (Olley 1973).

- 3 A low absorption region, where ($\alpha < 1 \text{ cm}^{-1}$), this region or tail mainly depends for its shape and magnitude on the purity, thermal history and preparation condition of the sample. This part is difficult to be studied due to very low absorption

3.6.1 First region absorption band

To calculate the optical band gap, E_{op} in this region, Eq. (7) is used. By plotting a graph between the energy in (eV) on the x-axis and $(\alpha h \lambda)^m$ on Y-axis. Now, m is as described can be either $1/2$, $2/3$, 2 or 3 according to the type of the transition. The band gap is the intersect on the y-axis of the extrapolated linear part of the graph. Where the slope of that linear part is the value of β .

To study the absorption band, we used the complex dielectric permittivity, $\epsilon^* = \epsilon_1 - i\epsilon_2$ where ϵ_1 and ϵ_2 are respectively the real and imaginary parts of the dielectric constant. By plotting ϵ_2 against the energy E then extrapolating the linear parts to the intercept on the Y-axis as illustrated in Fig. 13, the fundamental absorption band can be obtained.

Both real ϵ_1 and imaginary ϵ_2 parts of the dielectric constant are illustrated against wavelength in Fig. 12.

The imaginary part of the dielectric constant ϵ_2 , is a function of refractive index n and extinction coefficient k , as per the following equation:

$$\epsilon_2 = 2nK \tag{9}$$

and the real part of the dielectric constant, ϵ_1 , is also a function of refractive index n and extinction coefficient k , as pe the following equation:

$$\epsilon_1 = n^2 - K^2 \tag{10}$$

The real part of the dielectric constant is similar to its behavior to the refractive index which was expected given the direct relation in Eq. (10). As for the imaginary part, it shows clear decrease by increasing rGO.

Figure 13 shows the calculated values of ϵ_2 as a function of E (eV) for $rGO_xV_2O_5 \cdot nH_2O$ with different values of x . From Fig. 13 it is observed that there are two linear parts for the graphs and hence, two independent absorption bands. This indicates that $rGO_xV_2O_5 \cdot nH_2O$ nanocrystalline films have more than one type of conduction mechanism. Consequently, Eq. (12) may be applied next with the earlier knowledge of the optical gap.

By using the dielectric constant two parts ϵ_1 and ϵ_2 , the dissipation factor ($\tan \delta$) can be determined (El-Nahhas et al. 2012). It represents the power loss-rate of a mechanical

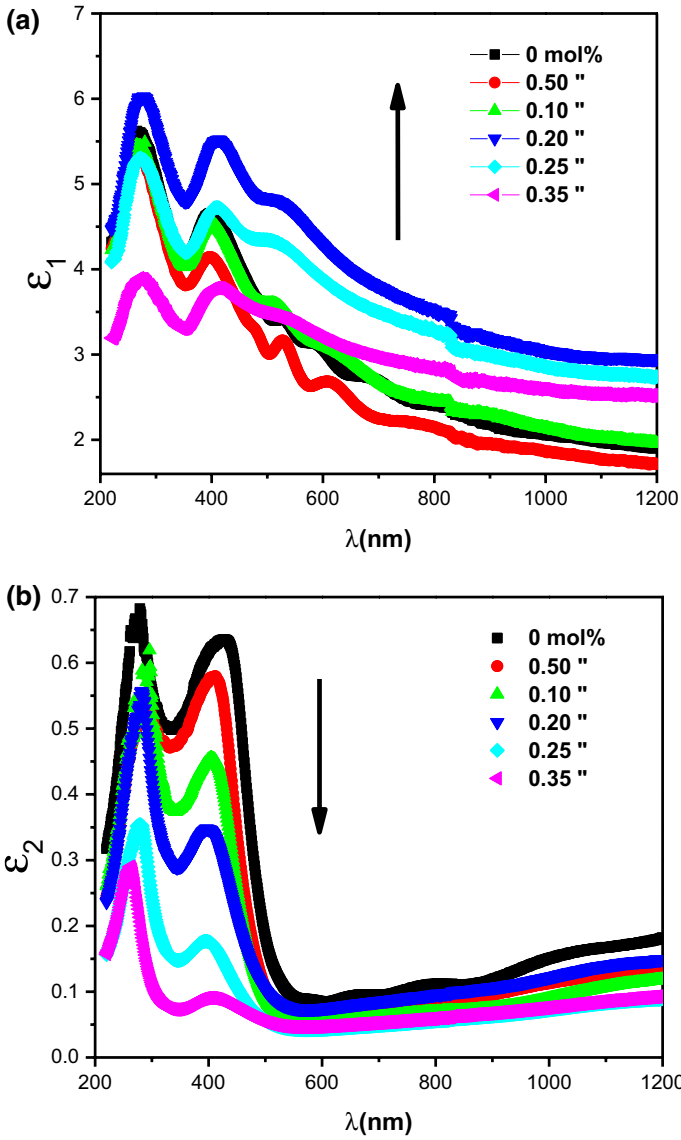


Fig. 12 **a** Real part of the dielectric (ϵ_1), **b** imaginary part of the dielectric (ϵ_2) constant against wavelength λ

mode, such as an oscillation in a dissipative system and is given by the following equation and illustrated in Fig. 14

$$\tan \delta = \frac{\epsilon_2}{\epsilon_1} \tag{11}$$

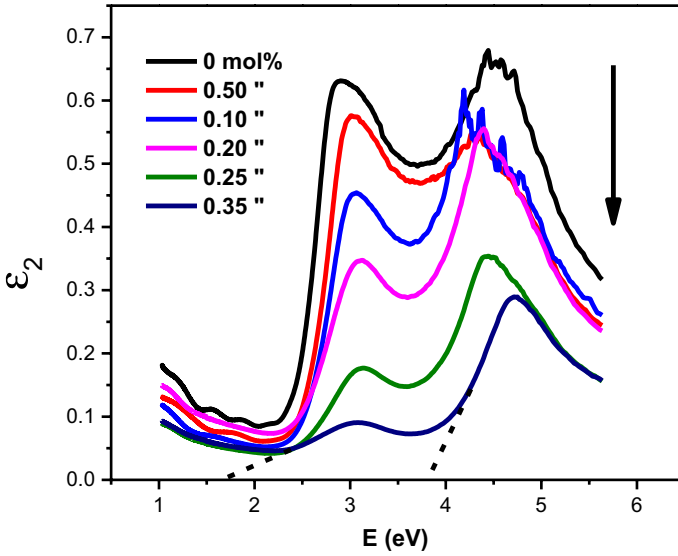


Fig. 13 Imaginary part of dielectric (ϵ_2) as a function of photon energy

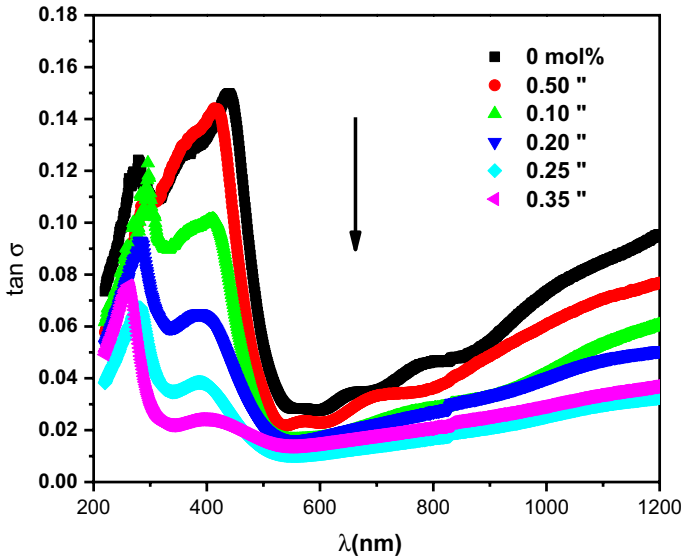


Fig. 14 The dissipation factor ($\tan \delta$) as a function of wavelength

The dissipation factor decreases with increasing of the r-GO. It is clearly that dissipation factor ($\tan \delta$) will also behave like the imaginary part of the dielectric constant which is expected as indicated in Eq. (11).

From the absorption data and absorption coefficient, we can see that $\alpha > 10^4$. Accordingly, our data is in the high-energy range where it obeys *Tauc's law* (Mott and Davis 2012; Pankove 1971).

The band gap of a material can be determined from a measurement of the absorption coefficient versus wavelength. If the bottom of the conduction band and the top of the valence band are assumed to have a parabolic shape, the absorption coefficient (α) can be expressed as follows:

$$\alpha = A \frac{(\hbar\nu - E_g)^m}{\hbar\nu} \quad (12)$$

Here, A is a constant and m depends on the nature of the optical transition (Al-Assiri et al. 2010; Ghobadi 2013):

- $m = 1/2$ for a direct allowed band gap
- $m = 2$ for an indirect allowed band gap
- $m = 3/2$ for a direct forbidden band gap
- $m = 3$ for an indirect forbidden band gap

The band gap for each optical transition type was investigated and listed in Table 3. It was also found that the direct band gap for pure vanadium is close to previous studies (Dultsev et al. 2006; Tashtoush and Kasasbeh 2013).

By using Eq. (12), all values of the optical band gaps for the four possible optical transition type were obtained and illustrated in Table 3. Then the regression coefficient was used to determine the most suitable transition type.

Figure 15a–d show the Indirect allowed band gap, direct allowed band gap, indirect forbidden band gap and direct forbidden band gap, respectively. Applying the results obtained from the absorption band (ϵ_2 vs. E of Fig. 13) it is noted that the first high energy band gives $E_{op2} \sim 2.656$ to 4.225 eV as given in Table 3. This is characterized by an indirect forbidden transition with $m = 3$, see Fig. 15c, while the second region for $\hbar\nu < 1.5$ eV is best presented by an absorption band with a gap of E_{op1} around 1.467 eV and $m = 3/2$, see Fig. 15d

To select the type of transition, the obtained values of band gaps in Table 3 were taken with regression varies from 0.995 to 0.998. The average regression suggests the direct forbidden transition to be the most suitable transition as it gives the highest

Table 3 Optical band gap for different concentrations of rGO

x (mol%)	0	0.05	0.10	0.20	0.25	0.35
Indirect allowed band gap 1 (IDA1)	2.175	2.321	2.342	2.015	2.299	1.628
Indirect allowed band gap 2 (IDA2)				3.129	3.315	3.468
Direct allowed band gap 1 (DA1)	2.384	2.588	2.537	2.260	2.015	
Direct allowed band gap 2 (DA2)	3.660	3.282	3.798	3.895	3.925	4.225
Indirect forbidden band gap 1 (IDF1)	2.180	2.195	2.204	2.051	2.099	1.719
Indirect forbidden band gap 2 (IDF2)			2.656	3.076	3.382	
Direct forbidden band gap 1 (DF1)	2.276	2.309	2.333	2.228	2.042	1.467
Direct forbidden band gap 2 (DF2)				3.237	3.359	3.704

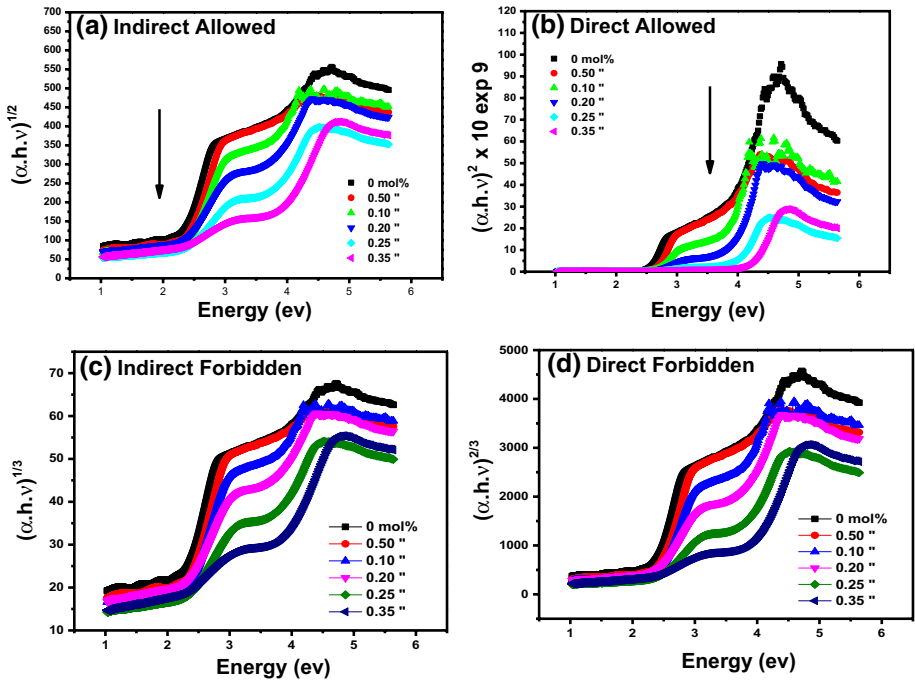


Fig. 15 **a** Indirect allowed band gap, **b** direct allowed band gap, **c** indirect forbidden band gap, **d** direct forbidden band gap

regression as indicated in Table 4 for $rGO_{0.25}V_2O_5 \cdot nH_2O$. Figure 16 shows the fitting process for determining E_{op1} and E_{op2} for representative $rGO_{0.25}V_2O_5 \cdot nH_2O$ sample.

Figure 17 shows the two obtained band gaps for direct forbidden transition. E_{op1} increases by adding rGO till reaching 0.10 mol% then, starting from 0.20 mol%, E_{op2} appears resulting in reducing E_{op1} while E_{op2} increases with the increase of rGO mol% (Tashtoush and Kasasbeh 2013). The variation in optical band gap associated with the addition of rGO, can be attributed to the change in the absorption coefficient due to increasing of layers intercalating between V_2O_5 layers.

Table 4 Optical band gap regression for 0.25rGO (mol%)

0.25 rGO mol%	Band gap	Regression "R"	R (average)
Indirect allowed band gap 1 (IDA1)	2.299	0.9976	0.99571
Indirect allowed band gap 2 (IDA2)	3.315	0.9939	
Direct allowed band gap 1 (DA1)	2.015	0.997	0.99523
Direct allowed band gap 2 (DA2)	3.925	0.9934	
Indirect forbidden band gap 1 (IDF1)	2.099	0.9985	0.99661
Indirect forbidden band gap 2 (IDF2)	3.076	0.9947	
Direct forbidden band gap 1 (DF1)	2.042	0.9986	0.99832
Direct forbidden band gap 2 (DF2)	3.359	0.998	

Bold value indicate the highest regression value

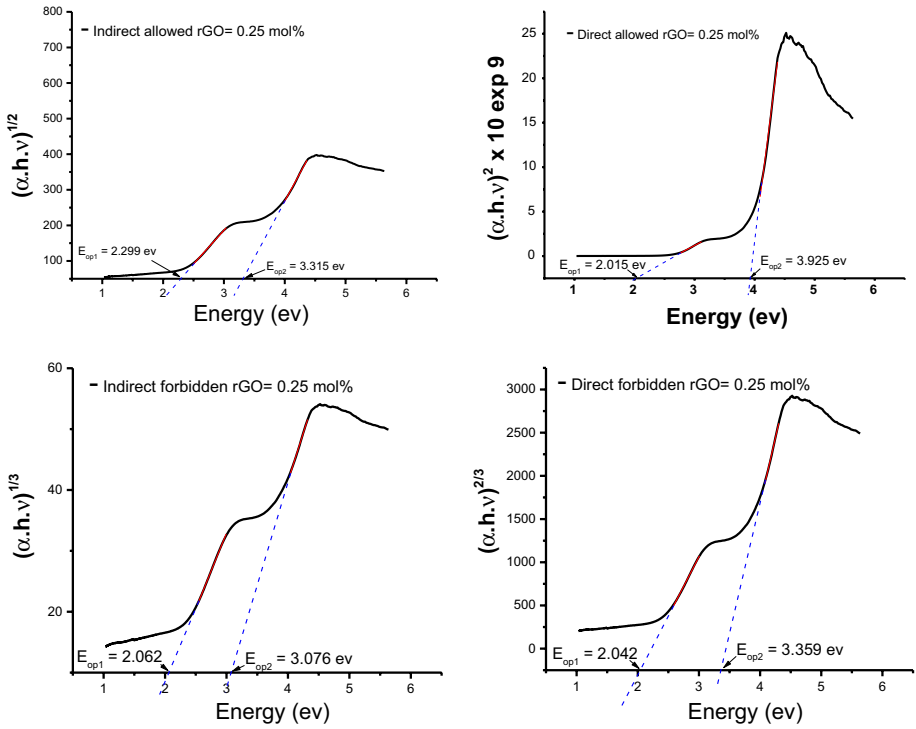


Fig. 16 Illustration for fitting to determine Eop1 and Eop2 for rGO_{0.25}V₂O₅·nH₂O

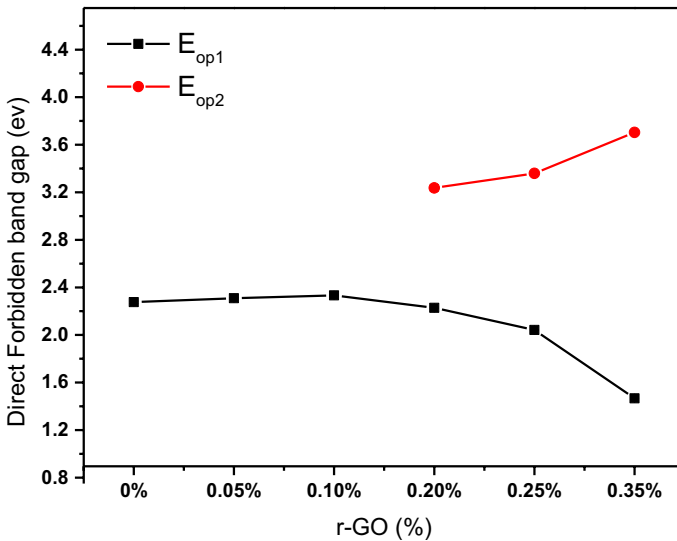


Fig. 17 The obtained results for Eop1 and Eop2 as a function of rGO content

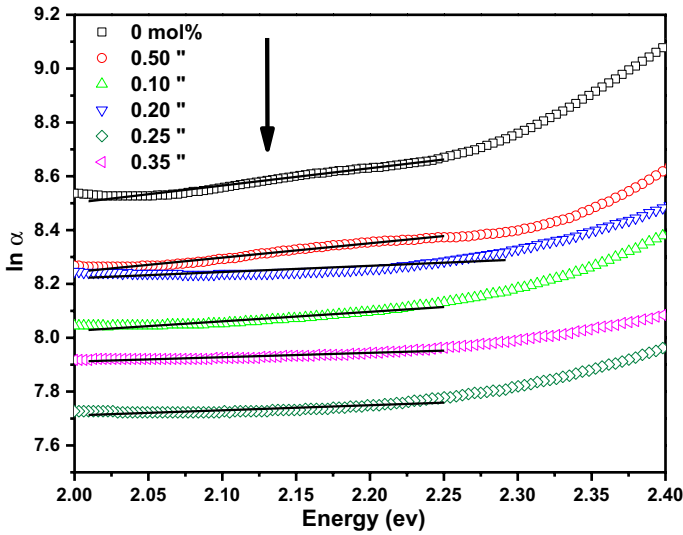


Fig. 18 Urbach tail for different rGO content

Table 5 Urbach energy for different rGO content

X(mol%)	0 mol%	0.05 mol%	0.10 mol%	0.20 mol%	0.25 mol%	0.35 mol%
Urbach energy (eV)	0.525	0.531	0.606	0.626	0.751	0.799

3.6.2 Second region: Urbach activation energy

Urbach activation energy or called the band tail, this region can be investigated in the low values of the absorption coefficient where $\alpha < 10^4 \text{ cm}^{-1}$. Because this region is in at low photon energy, it is usually following Urbach’s rule (Mott and Davis 2012; Khan and Hogarth 1991). The Urbach’s rule is described in Equation (8), where E_c is Urbach’s energy and α_0 is constant, the Urbach’s energy represents the width of the localized states of the conduction band (band tail states). In general, the Urbach energy represents the amount of damage due to disorder in an amorphous or nanocrystalline semiconductor. The absorption in this region is caused by optical transitions between localized states in the middle of the gap and extended states in the conduction or valence band.

Urbach energy was calculated using the equation below (Bahgat et al. 2005; Studenyak et al. 2014)

$$\alpha = B \exp (h\nu/E_c) \text{ for } h\nu < E_g \tag{13}$$

Plotting $\ln \alpha$ as a function of $h\nu$, as shown in Fig. 18, by plotting $\ln (\alpha)$ and the incident photon energy ($h\nu$), a straight portion appears. The slope of this line is the value of E_c (Morigaki and Ogihara 2017).

The values were calculated and listed in Table 5. It is clear from Table 5 that the Urbach energy increases with the increase of rGO. This can be explained by the increase of the degree of disorder due to more localized states as a result of adding rGO.

3.7 Dispersion energy parameters and effective mass

The calculated refractive index can then be used in the following simple oscillator model proposed by Wemple–DiDomenico (WDD) (González-Leal 2013; Yakuphanoglu et al. 2004) as shown in Eq. (14)

$$n^2 - 1 = \frac{E_d E_o}{E_o^2 - (h\nu)^2} \tag{14}$$

where E_o is the energy of a single oscillator and E_d is the energy of dispersion. Both of these energy values can be calculated by modifying Eq. (15) as follows:

$$(n^2 - 1)^{-1} = \frac{E_o}{E_d} - \frac{1}{E_o E_d} (h\nu)^2 \tag{15}$$

Then, by plotting $(n^2 - 1)^{-1}$ versus $(h\nu)^2$, Fig. 19, it is possible to calculate $(E_o E_d)^{-1}$ (i.e., the slope) and E_o/E_d (i.e., the y intercept) from the linear regression in the area with this behavior.

The oscillator energy E_o and dispersion energy E_d are obtained from the slope $(E_o E_d)^{-1}$ and intercept E_o/E_d on the vertical axis of the straight-line portion of $(n^2 - 1)^{-1}$ versus $(h\nu)^2$ plot, respectively listed in Table 6.

Furthermore, the single oscillator parameters E_o and E_d is related to the imaginary part of dielectric constant (ϵ_2) which include the desired response information about electronic and optical properties of the material. Thus, the determination of imaginary dielectric constant moments is important. The M_1 and M_3 moments of the optical

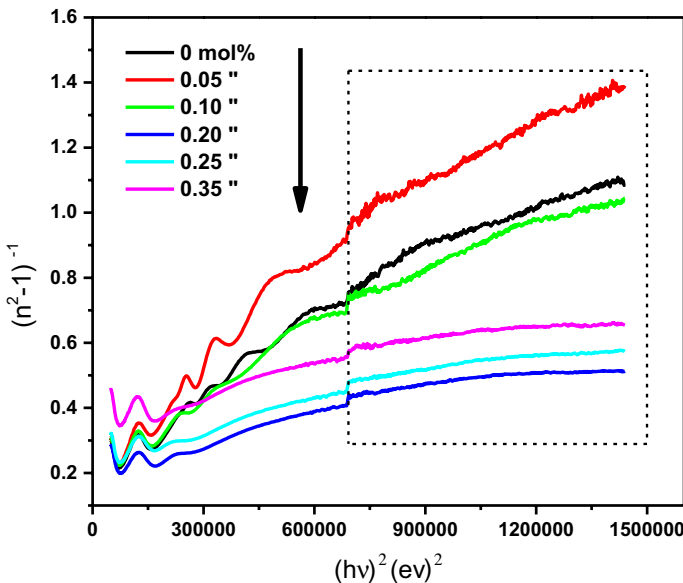


Fig. 19 Plotting $(n^2 - 1)^{-1}$ versus $(h\nu)^2$ showing straight lines intersecting with y-axis

Table 6 Dispersion energy parameters, effective mass and inter-atomic distance

X (mol%)	$E_0 \times 10^3$	$E_d \times 10^3$	M_{-1}	$M_{-3} \times 10^{-6}$	ϵ_{∞}	$N_l/m^* \times 10^{37}$	m^*/m_e	$N_l \times 10^{22} (m^{-3})$	n_0	R (nm)
0	1.17	2.16	1.84	1.34	2.60	5.08	2.41	1.11	1.61	44.80
0.05	1.02	1.73	1.70	1.64	2.29	4.13	3.02	1.14	1.51	44.47
0.10	1.02	2.29	2.25	0.22	2.73	5.60	2.28	1.16	1.65	44.15
0.20	2.09	5.31	2.54	0.58	3.55	4.58	2.89	1.21	1.88	43.57
0.25	1.91	4.55	2.39	0.66	3.34	4.44	3.05	1.23	1.83	43.30
0.35	2.41	4.51	1.87	0.32	2.88	2.69	5.20	1.28	1.70	42.80

spectrum (Al-Assiri et al. 2010; Nwofe et al. 2012) are given by $E_o^2 = \frac{M_{-1}}{M_{-3}}$ and $E_d^2 = \frac{M_{-1}^3}{M_{-3}}$. The final calculated moments M_1 and M_3 are listed in Table 6.

The obtained data of refractive index n can be further analyzed to obtain the high-frequency dielectric constant ϵ_∞ according to the following procedure. According to Pankove (1971), this procedure describes the contribution of the free carriers and the lattice vibrational modes of the dispersion energy as presented in Eq. (16)

$$\epsilon_1 = \epsilon_\infty - \frac{e^2 N_t}{\pi \epsilon_o m^* C^2} \lambda^2 \tag{16}$$

where ϵ_o is the lattice dielectric constant, λ is the wavelength, e is the electron charge, N_t is the free charge-carrier concentration, ϵ_o is the permittivity of the free space, m^* is the charge carriers effective mass in kg, and c is the speed of light. Figure 19 illustrates the plotted graph of the real dielectric constant ϵ_1 with the λ^2 . Where it shows the relation is linear at higher wavelengths (Mady et al. 2012). The extrapolation of these linear parts on the y-axis gives the value of ϵ_∞ as shown in Fig. 20. Then, from the slope of these linear parts, we can deduce the value of N_t/m^* for the prepared nanocrystalline films for different rGO concentrations (Abdel-Aziz et al. 2006). Values of ϵ_∞ and N_t/m^* are given in Table 6.

Due to the insertion of electrons from rGO into the $V_2O_5 \cdot nH_2O$ nanocrystalline films, the electron concentration N_c in the prepared nanocrystalline films increased and increasing with it the Fermi level to be near the bottom of the conduction band. According to Mott criterion (Mott 2004), there is a critical electron concentration value N_c , that if the concentration is larger than it, the Fermi level enters the conduction band. This value can be calculated as following Eq. (17)

$$N_c^{1/3} a^* \approx 0.25 \tag{17}$$

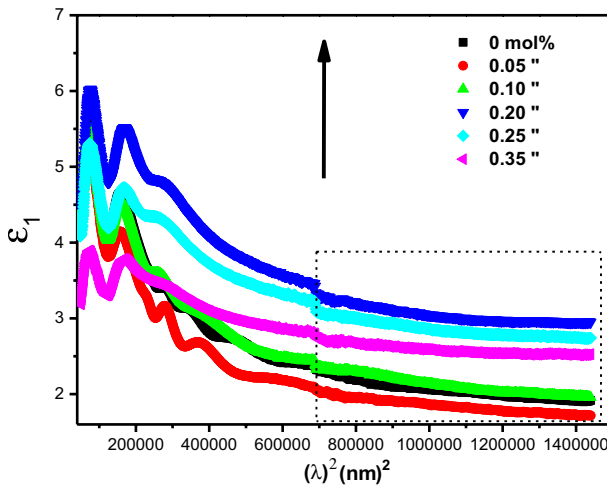


Fig. 20 Real part of the dielectric constant (ϵ_1) as a function of λ^2

where a^* can be expressed as $a^* = a_0 \epsilon_r (m_e / m^*)$, a_0 is the effective Bohr radius, ϵ_r is the dielectric constant of the host lattice, m_e is free electron mass and m^* is the effective charge carrier mass.

The free charge carriers inter-atomic distance is given by using the present data where it can be calculated using the following Eq. (18). These parameters are calculated and listed in Table 6.

$$R = \frac{1}{N_t^{1/3}} \tag{18}$$

3.8 The volume and surface energy loss

The volume energy loss function (VELF) and the surface energy loss function (SELF) are computed using Eq. (19) and Eq. (20), respectively (Ammar et al. 2002) and as illustrated in Figs. 21 and 22 respectively:

$$VELF = \epsilon'' / (\epsilon''^2 + \epsilon'^2) \tag{19}$$

$$SELF = \epsilon'' / (\epsilon''^2 + (\epsilon' + 1)^2) \tag{20}$$

In general, both surface (SELF) and volume (VELF) energy loss decreases by the increase of rGO. Also, it is obvious that the surface energy loss function values are smaller than volume energy loss function. This can be explained as the energy loss is a result of inter-band electronic transition in the interior of the nanocrystalline films (Ali et al. 2013).

Fig. 21 Volume energy loss with rGO content

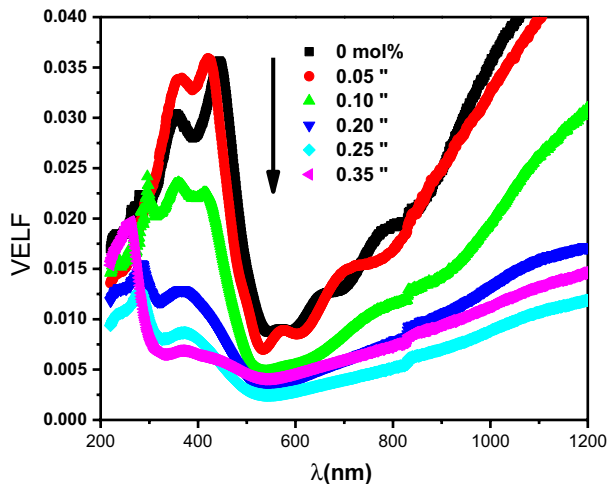
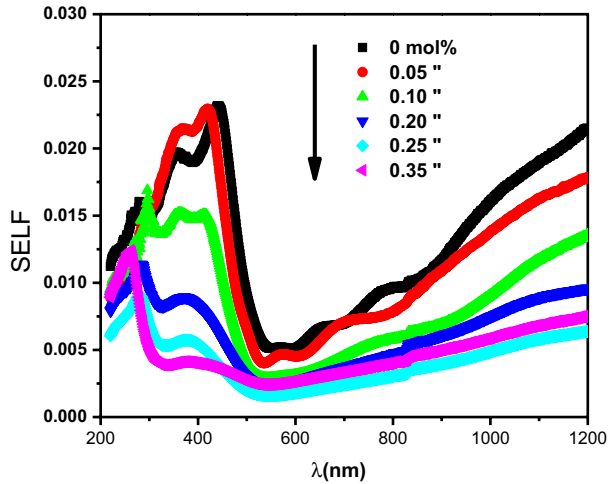


Fig. 22 Surface energy loss with rGO content



4 Conclusion

Nanocrystalline films of $x\text{rGO}$ ($x-1$) $\text{nH}_2\text{OV}_2\text{O}_5$ ($0 \leq x \leq 0.35$) were prepared by the sol-gel technique. Optical constants such as absorption coefficient (α) and band tail (E_a), extinction coefficient (k), refractive index (n), dielectric constant (ϵ), loss factor ($\tan \delta$), volume (VELF) and surface (SELF) energy loss functions were calculated. XRD showed that the obtained films are nanocrystalline with the particle size 4.9–3.2 nm. Optical measurements revealed that there are two different optical gaps present. E_{op1} and E_{op2} suggests an indirect forbidden transition with optical gap in the range 1.719–2.180 eV and 2.656–3.382 eV, respectively. Wemple–Didomenico single effective oscillator model was used to study the dispersion of films refractive index. Relating the real part of the optical dielectric function led to the calculation of the charge carrier concentration and their effective mass. In the UV region, the absorbance curve was not showing any shifting with the increase of the r-GO and absorbance shoulder still detected for wave lengths lower than 500 nm. Finally, we conclude that this film is a good candidate for solar cell photostabilizer applications.

References

- Abdel-Aziz, M., Yahia, I., Wahab, L., Fadel, M., Afifi, M.: Determination and analysis of dispersive optical constant of TiO_2 and Ti_2O_3 thin films. *Appl. Surf. Sci.* **252**, 8163–8170 (2006)
- Abyazisani, M., Bagheri-Mohagheghi, M.M., Benam, M.R.: Study of structural and optical properties of nanostructured V_2O_5 thin films doped with fluorine. *Mater. Sci. Semicond. Process.* **31**, 693–699 (2015)
- Al-Assiri, M., El-Desoky, M., Alyamani, A., Al-Hajry, A., Al-Mogeeth, A., Bahgat, A.: Spectroscopic study of nanocrystalline $\text{V}_2\text{O}_5\text{-nH}_2\text{O}$ films doped with Li ions. *Opt. Laser Technol.* **42**, 994–1003 (2010)
- Ali, A., Son, J., Ammar, A., Moez, A.A., Kim, Y.: Optical and dielectric results of $\text{Y}_0.225\text{Sr}_{0.775}\text{CoO}_3 \pm \delta$ thin films studied by spectroscopic ellipsometry technique. *Results Phys.* **3**, 167–172 (2013)
- Ammar, A., El-Sayed, B., El-Sayad, E.: Structural and optical studies on ortho-hydroxy acetophenone azine thin films. *J. Mater. Sci.* **37**, 3255–3260 (2002)

- Arefinia, Z., Asgari, AJPEL-dS, Nanostructures: Novel attributes in the scaling and performance considerations of the one-dimensional graphene-based photonic crystals for terahertz applications. *Physica E: Low-dimens. Syst. Nanostruct.* **54**, 34–39 (2013)
- Aristizábal, A., Mikan, M.: Optical properties of CDS films by analysis of spectral transmittance. *IOSR J. Appl. Phys.* **8**, 24–31 (2016)
- Bahgat, A., Ibrahim, F., El-Desoky, M.: Electrical and optical properties of highly oriented nanocrystalline vanadium pentoxide. *Thin Solid Films* **489**, 68–73 (2005)
- Bahgat, A., Ibrahim, F., El-Desoky, M.: Nanocrystalline vanadium pentoxide xerogel properties and hydrogen sensing. In: AIP Conference Proceedings, pp. 61–67 (2011)
- Bartram, S.F., Kaelble, E.F.: *Handbook of X-Rays for Diffraction, Emission, Absorption and Microscopy*, pp. 17.1–17.18. McGraw-Hill, New York (1967)
- Brownson, D.A., Kampouris, D.K., Banks, C.E.J.C.S.R.: Graphene electrochemistry: fundamental concepts through to prominent applications. *J. Chem. Soc. Rev.* **41**, 6944–6976 (2012)
- Caglar, M., Caglar, Y., Ilcan, S.: The determination of the thickness and optical constants of the ZnO crystalline thin film by using envelope method. *J. Optoelectron. Adv. Mater.* **8**, 1410–1413 (2006)
- Dultsev, F., Vasilieva, L., Maroshina, S., Pokrovsky, L.: Structural and optical properties of vanadium pentoxide sol–gel films. *Thin Solid Films* **510**, 255–259 (2006)
- El-Desoky, M., El-Barbary, G., El Refaay, D., El-Tantawy, F.: Optical constants and dispersion parameters of La-doped ZnS nanocrystalline films prepared by sol–gel technique. *Optik* **168**, 764–777 (2018)
- El-Nahas, M., Abdel-Khalek, H., Salem, E.: Optical properties of 3, 4, 9, 10-perylenetetra-carboxylic diimide (PTCDI) organic thin films as a function of post-annealing temperatures. *Am. J. Mater. Sci.* **2**, 131–137 (2012)
- Ganeshan, S., Ramasundari, P., Elangovan, A., Vijayalakshmi, R.: Optical and structural studies of vanadium pentoxide thin films. *Наносистемы: физика, химия, математика* **7**, 687–690 (2016)
- Ghamsari, B.G., Tosado, J., Yamamoto, M., Fuhrer, M.S., Anlage, SMJSr: Measuring the complex optical conductivity of graphene by fabry-pérot reflectance spectroscopy. *Sci. Rep.* **6**, 34166 (2016)
- Ghobadi, N.: Band gap determination using absorption spectrum fitting procedure. *Int. Nano Lett.* **3**, 1–4 (2013)
- González-Leal, J.: The Wemple–DiDomenico model as a tool to probe the building blocks conforming a glass. *Physica Status Solidi (b)* **250**, 1044–1051 (2013)
- Gupta, P., Ramrakhiani, M.: Influence of the particle size on the optical properties of CdSe nanoparticles. *Open Nanosci. J.* **3**, 15–19 (2009)
- Kazakova, E., Berezina, O., Kirienko, D., Markova, N.: Vanadium oxide gel films: optical and electrical properties, internal electrochromism and effect of doping. *J. Sel. Top. Nano Electron. Comput.* **2**, 7–19 (2014)
- Khan, G., Hogarth, C.: Optical absorption spectra of evaporated V_2O_5 and co-evaporated V_2O_5/B_2O_3 thin films. *J. Mater. Sci.* **26**, 412–416 (1991)
- Klein, L.C.: *Sol–Gel Optics: Processing and Applications*, vol. 259. Springer, Berlin (2013)
- Lee, M., Balasingam, S.K., Ko, Y., Jeong, H.Y., Min, B.K., Yun, Y.J., Jun, Y.: Graphene modified vanadium pentoxide nanobelts as an efficient counter electrode for dye-sensitized solar cells. *Synth. Met.* **215**, 110–115 (2016a)
- Lee, S.-W., Kim, S., Bae, S., Cho, K., Chung, T., Mundt, L.E., Lee, S., Park, S., Park, H., Schubert, MCJSr: UV degradation and recovery of perovskite solar cells. *Sci. Rep.* **6**, 38150 (2016b)
- Legendre, J.-J., Aldebert, P., Baffier, N., Livage, J.: Vanadium pentoxide gels: II structural study by X-ray diffraction. *J. Colloid Interface Sci.* **94**, 84–89 (1983)
- Li, L., Lu, J., Li, R., Shen, C., Chen, Y., Yang, S., Gao, X.: The determination of the thickness and optical constants of the microcrystalline silicon thin film by using envelope method. *Optoelectron. Adv. Mater. Rapid Commun.* **3**, 625–630 (2009)
- Li, Z., Gong, F., Zhou, G., Wang, Z.-S.: NiS₂/reduced graphene oxide nanocomposites for efficient dye-sensitized solar cells. *J. Phys. Chem. C* **117**, 6561–6566 (2013)
- Li, Z., Sun, H., Xu, J., Zhu, Q., Chen, W., Zakharova, G.S.: The synthesis, characterization and electrochemical properties of $V_3O_7 \cdot H_2O/CNT$ nanocomposite. *Solid State Ion.* **262**, 30–34 (2014)
- Mady, H.A., Negm, S.E., Moghny, A.A., Abd-Rabo, A., Bahgat, A.: Study of optical properties of highly oriented nanocrystalline $V_2O_5 \cdot nH_2O$ films doped with K ions. *J. Sol Gel Sci. Technol.* **62**, 18–23 (2012)
- Matkovic, A., Gajic, R.: Spectroscopic imaging ellipsometry of graphene. *SPIE Newsroom* **1**, 1–4 (2013)
- McNulty, D., Noel Buckley, D., O'Dwyer, C.: NaV_2O_5 from sodium ion-exchanged vanadium oxide nanotubes and its efficient reversible lithiation as a li-ion anode material. *ACS Appl. Energy Mater.* **2**, 822–832 (2019)

- Morigaki, K., Ogihara, C.: Amorphous semiconductors: structure, optical, and electrical properties. In: Springer Handbook of Electronic and Photonic Materials, pp. 1. Springer, Cham (2017)
- Mott, N.: Metal-Insulator Transitions. CRC Press, Boca Raton (2004)
- Mott, N.F., Davis, E.A.: Electronic Processes in Non-Crystalline Materials. Oxford University Press, Oxford (2012)
- Nagaraju, D.H., Wang, Q., Beaujuge, P., Alshareef, H.N.: Two-dimensional heterostructures of V_2O_5 and reduced graphene oxide as electrodes for high energy density asymmetric supercapacitors. *J. Mater. Chem. A* **2**, 17146–17152 (2014)
- Nwofe, P., Reddy, K.R., Tan, J., Forbes, I., Miles, R.: Thickness dependent optical properties of thermally evaporated SnS thin films. *Phys. Procedia* **25**, 150–157 (2012)
- Olley, J.J.S.S.C.: Structural disorder and the Urbach edge. *Solid State Commun.* **13**, 1437–1440 (1973)
- Pankove, J.: Absorption. In: IEEE (ed) Optical Processes in Semiconductors, pp. 34–86. Prentice-Hall, Inc, Englewood Cliffs (1971)
- Pergament, A., Kazakova, E., Stefanovich, G.: Optical and electrical properties of vanadium pentoxide xerogel films: modification in electric field and the role of ion transport. *J. Phys. D Appl. Phys.* **35**, 2187–2197 (2002)
- Prociow, E., Zielinski, M., Sieradzka, K., Domaradzki, J., Kaczmarek, D.: Electrical and optical study of transparent V-based oxide semiconductors prepared by magnetron sputtering under different conditions. *Radioengineering* **20**, 204–208 (2011)
- Ramana, C., Hussain, O., Naidu, B.S., Reddy, P.: Spectroscopic characterization of electron-beam evaporated V_2O_5 thin films. *Thin Solid Films* **305**, 219–226 (1997)
- Randviir, E.P., Brownson, D.A., Banks, C.E.: A decade of graphene research: production, applications and outlook. *Mater. Today* **17**, 426–432 (2014)
- Roose, B., Baena, J.-P.C., Gödel, K.C., Graetzel, M., Hagfeldt, A., Steiner, U., Abate, A.J.N.E.: Mesoporous SnO_2 electron selective contact enables UV-stable perovskite solar cells. *J. Nano Energy* **30**, 517–522 (2016)
- Roose, B., Johansen, C.M., Dupraz, K., Jaouen, T., Aebi, P., Steiner, U., Abate, A.J.N.E.: A Ga-doped SnO_2 mesoporous contact for UV stable highly efficient perovskite solar cells. *J. Mater. Chem. A* **6**, 1850–1857 (2018)
- Sánchez-González, J., Díaz-Parralejo, A., Ortiz, A., Guiberteau, F.: Determination of optical properties in nanostructured thin films using the Swanepoel method. *Appl. Surf. Sci.* **252**, 6013–6017 (2006)
- Schmiedova, V., Pospisil, J., Kovalenko, A., Ashcheulov, P., Fekete, L., Cubon, T., Kotrusz, P., Zmeskal, O., Weiter, M.J.J.o.N.: Physical properties investigation of reduced graphene oxide thin films prepared by material inkjet printing. *J. Nanomater.* **2017**, 1–8 (2017)
- Studenyak, I., Kranjčec, M., Kurik, M.: Urbach rule in solid state physics. *Int. J. Opt. Appl.* **4**, 96–104 (2014)
- Takeda, S., Kawakita, Y., Inui, M., Maruyama, K., Tamaki, S., Sugiyama, K., Waseda, Y.: Structure and dynamical properties of molten V_2O_5 . *J. Non-Cryst. Solids* **205**, 151–154 (1996)
- Tashtoush, N.M., Kasasbeh, O.: Optical properties of vanadium pentoxide thin films prepared by thermal evaporation method. *Jordan J. Phys.* **6**, 7–15 (2013)
- Wang, G., Zhang, Y., You, C., Liu, B., Yang, Y., Li, H., Cui, A., Liu, D., Yan, H.: Two dimensional materials based photodetectors. *Infrared Phys. Technol.* **88**, 149–173 (2018)
- Wright, A.C.: The structure of vitreous and liquid V_2O_5 . *Philos. Mag. B* **50**, L23–L28 (1984)
- Yakuphanoglu, F., Cukurovali, A., Yilmaz, I.: Single-oscillator model and determination of optical constants of some optical thin film materials. *Physica B: Condens. Matter* **353**, 210–216 (2004)
- Yao, T., Oka, Y.: On the layer structure of vanadium pentoxide gels Comment on “Molecular dynamic simulation of the vanadium pentoxide gel host”. *Solid State Ion.* **96**, 127–128 (1997)
- Zhao, Y., Chen, F., Shen, Q., Zhang, L.J.Ao: “Light-trapping design of graphene transparent electrodes for efficient thin-film silicon solar cells. *J. Appl. Opt.* **51**, 6245–6251 (2012)
- Zheng, S., Tu, Q., Urban, J.J., Li, S., Mi, B.: Swelling of graphene oxide membranes in aqueous solution: characterization of interlayer spacing and insight into water transport mechanisms. *ACS Nano* **11**, 6440–6450 (2017)